



The Effect of Moisture Intake on the Mode-II Dynamic Fracture Behavior of Carbon Fiber/Epoxy Composites

R. Chavez Morales¹ · V. Eliasson¹

Received: 16 May 2020 / Accepted: 29 July 2020 / Published online: 10 August 2020
© Society for Experimental Mechanics, Inc 2020

Abstract

An experimental investigation of the mode-II dynamic fracture behavior of carbon fiber/epoxy composites when exposed to moisture intake in excess of 1 wt% was conducted. In particular, one goal was to investigate if the different moisture intake methods result in different dynamic fracture responses. Experiments were performed by launching a projectile from a gas gun onto pre-notched unidirectional carbon fiber/epoxy rectangular specimens manufactured in-house. Additionally, the material was characterized in-house to account for material property degradation due to water intake. Two different aging techniques were used to obtain the desired moisture contents. First, hygrothermal aging was used to obtain 1.5 wt% moisture uptake by having samples submerged in water at 65 °C. Second, submersion in water at room temperature was used to obtain the same effect, resulting in longer soaking times. Ultra high-speed photography combined with digital image correlation were used to extract stress intensity factors from each experiment. The experiment successfully obtained dominant mode-II loading of the crack. It was found that carbon fiber/epoxy samples with no significant moisture content had a higher mode-II critical stress intensity factor compared to samples that were aged. Additionally, no significant differences were found between the different types of aging techniques.

Keywords Dynamic fracture · Digital image correlation · Carbon fiber · Mode-II · Ultra high-speed · Aging

Introduction

Ever since the end of World War II, composite materials have started to replace certain traditional metallic naval structures. Mine sweepers are the most clear example of this trend, which adopt composite construction due to their non-conductive properties. Overall, there has been an increase in hull sizes of composite built ships as time has passed [17]. A modern example of a ship employing a fully composite design can be observed in the Visby Class corvette of the Swedish navy, which employed this design path for stealth purposes [13]. Reasons to adopt a fiber reinforced composite design include but are not limited to: high strength-to-weight ratio, low magnetic, infrared and radar signatures, the ability to manufacture complex shapes, and rust resistance [17].

However, naval structures are constantly exposed to ocean water, a highly hostile environment. Water absorption can

have detrimental effects on fiber reinforced composite materials, such as matrix swelling, reduction in the glass transition temperature, matrix plasticization, surface degradation and blistering, and degradation of material properties [3, 5, 15]. However, up until now, most studies in the area of moisture intake of composites have been conducted under quasi-static conditions. Naval structures will not be limited to such conditions, with a notable example being wave slamming, which can afflict any ship. Notable studies conducted under dynamic and aquatic conditions include those performed by Matos et al. [15], Shillings et al. [21] and Arora et al. [2], which deal with blast in aquatic conditions.

Research focused solely on the dynamic fracture behavior of composites is still ongoing with a focus on topics covering how blast loading can affect different types of composites [1, 2, 8, 15, 18, 21, 23], difference between penetration damage vs. blast damage in composites [16], and in-plane dynamic fracture behavior of composite materials [4, 10–12, 14, 19]. However, to the best knowledge of the authors, there has not been a significant amount of research available in open literature relating water intake and the fracture behavior of composite materials. Therefore, a study was conducted to

✉ V. Eliasson
eliasson@ucsd.edu

¹ Department of Structural Engineering, University of California, San Diego, La Jolla, CA 92093-0085, USA

evaluate how the dynamic fracture behavior of carbon fiber reinforced composites is affected by moisture intake.

Here, the experimental setup being used is similar to the ones used by Coker and Rosakis [4] and Kalthoff et al. [7]. This setup allows for dynamic mode-II loading of a single edge notch specimen using a gas gun as a loading device. A projectile is launched from the gas gun to perform edge-on impact on carbon fiber/epoxy samples. Notched unidirectional carbon fiber/epoxy samples with moisture intake (> 1 wt%) were dynamically loaded and their fracture response was compared to samples with no significant moisture intake. The goal was to obtain the critical mode-II stress intensity factors of the notched carbon fiber/epoxy samples to observe if the variation in moisture intake resulted in a different dynamic response.

To achieve this goal ultra high-speed photography was used to record the fracture event. The obtained footage was then analyzed with digital image correlation (DIC) to obtain the full-field displacements around the samples' crack-tips. By using a continuum fracture mechanics model relating displacements and stress intensity factors, a least-squares regression analysis was performed and the stress intensity factors were obtained. Thus, dynamic stress intensity factor histories were obtained for all types of samples, and differences between samples that have been exposed to water uptake and those who have not were studied.

In addition, it was of interest to better understand if different aging processes produced different dynamic responses of the samples. As such, two types of aging processes were used to achieve the desired moisture contents. Samples were subjected to (1) hygrothermal aging using distilled water in which they achieved the desired moisture content in one month, and (2) samples were naturally aged by submerging them in distilled water at room temperature for over one year. Even though researchers have used hygrothermal aging with great success, no comparison study was found when dealing with dynamic fracture and as such this was investigated as well.

It must be noted that in reality special coatings would be applied to composite structures in service. However such coatings can be damaged during service. As such, different degrees of moisture absorption would be appreciated. The results presented here display a worst case scenario where the material is fully submerged with no coatings applied to it.

A problem when studying dynamic crack growth is to properly determine the tip location of a growing crack and thus establish the moment of crack growth initiation. The reason this is a challenge is due to the limited spatial resolution often found in ultra high-speed cameras, which makes visual identification of the crack-tip location difficult. As such, in this study, the magnitude of the displacements and the shear strains in the area surrounding the crack-tip were

tracked during the impact event to determine the instant of crack growth.

Material

All experimental samples consisted of unidirectional carbon fiber/epoxy cut into rectangular shapes. Unidirectional T-700 carbon fibers plies were infused with SC-780 infusion epoxy obtained from Kaneka Aerospace. Carbon fiber was chosen due to its popular use in commercial applications and availability. Using a carbon fiber/epoxy laminate allowed for comparison with previous results obtained by Coker and Rosakis [4], which also used carbon fiber/epoxy laminates with the same layup. However, it must be noted that the type of carbon fibers and epoxy, and laminate thickness used by Coker and Rosakis were different than the one chosen for the present study.

Manual layups were performed to create rectangular plates 16-ply thick, resulting in a sample thickness of 2 mm. Smaller samples with dimensions 127 mm × 203 mm were obtained from the plate by segmenting it with a saw equipped with a diamond blade. All the fibers in the sample were oriented along the short end. Following this, a thin notch was machined at the middle of the long end and was oriented along the fiber direction as shown in Fig. 1. A sharp razor blade was then used to create a small crack at the end of the notch.

A total of 12 samples were divided into three groups: (1) samples that were desiccated to have negligible moisture content will be referred to as the *dry samples*; (2) samples that were subjected to hygrothermal aging to become saturated with water will be referred to as the *soaked samples*. Hygrothermal aging was obtained by fully submerging the samples in a water tank kept at 65 °C by immersing a heater to the water tank. Increasing the water temperature is what makes hygrothermal aging possible, allowing for water saturation in a timely fashion [3, 21]. In this case the samples attained a moisture saturation content of 1.56 wt% in 38 days. And, (3) samples left in a water container at room temperature for an extended period of time. These samples will be referred to as the *naturally aged samples*. These samples were left in the water container for 400 days until they achieved a saturation content of 1.5 wt%.

The naturally aged group was created to observe if there was any difference between the different aging methods when subject to dynamic fracture. In particular, with hygrothermal aging submersion time is decreased by increasing temperature which some research has hinted at the possibility of leading to further degradation in material performance [6]. The authors wanted to explore if time and temperature had an effect on the dynamic behavior of carbon fiber/epoxy

Fig. 1 Mode-II experimental setup. Impact occurs from left toright

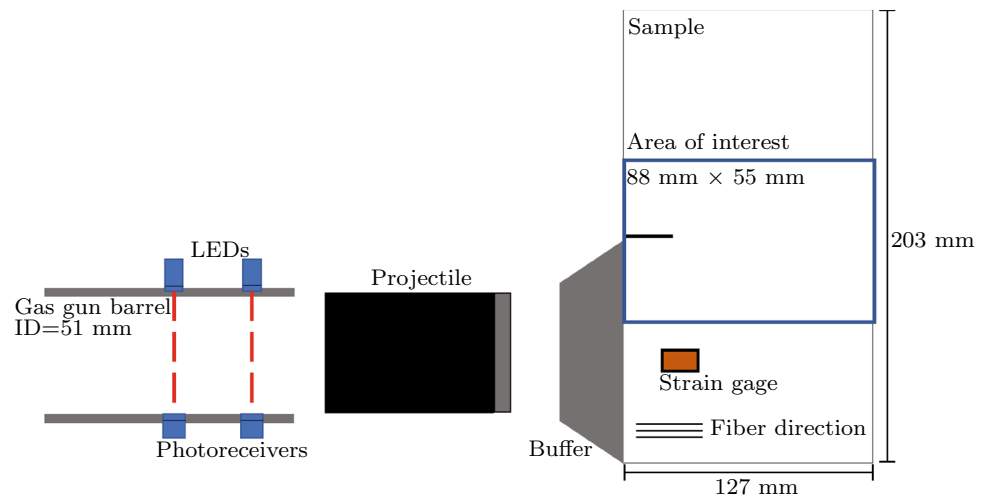


Table 1 Carbon fiber/epoxy material properties in dry and soaked conditions

	Dry	Soaked (hygrothermally aged)	Difference
E_1	153.5 ± 8 GPa	150.7 ± 7 GPa	n/a
E_2	10.2 ± 0.8 GPa	8.6 ± 0.6 GPa	10%
G_{12}	7.6 ± 0.5 GPa	5.8 ± 0.2 GPa	25%
ν_{12}	0.4 ± 0.05	0.35 ± 0.05	n/a

for this type of experiment, by creating a less aggressive aging environment.

The material manufactured was characterized in both dry and soaked conditions to obtain the Young's modulus along the fiber direction, E_1 , the Young's modulus along the transverse direction, E_2 , the in-plane shear modulus, G_{12} , and the Poisson's ration, ν_{12} . Tensile coupons were manufactured according to ASTM standards D3039/D3039M-17 and D3518/D3518M-13. The coupons were divided into two groups with one group being desiccated and the other being hygrothermally aged before being characterized. As shown in Table 1, the fiber dominated material properties, E_1 , did not experience any significant changes between dry and soaked conditions, as expected. However, the matrix dominated properties, E_2 and G_{12} , experienced a degradation of 10% and 25% respectively.

Experimental Setup

Edge-on impacts were performed on the rectangular notched samples. Delrin rods were cut into right cylindrical projectiles, 76 mm long and 51 mm in diameter. A 3.175 mm thick steel disk was bonded to the leading edge of the projectile. Then, the projectiles were launched from a pressurized air

gun to create an impact load onto the sample. The projectile impacted onto a steel buffer bonded to the bottom half of the sample, Fig. 1. Upon impact the buffer redistributed the load below the notch, leading to asymmetrical loading of the notch, and consequently resulting in mode-II fracture conditions. Additionally, the buffer prevented fiber crushing upon impact, which could hinder the proper implementation of DIC depending on the extent of damage.

The gas gun was fitted with a velocity sensor consisting of two pairs of light emitting diodes (LEDs), and photodiode receivers in order to monitor the projectile speed and ensure constant impact conditions, Fig. 1. In the present study, the projectiles were launched at a velocity of 52 m/s.

The sample was placed inside a catcher box to ensure that all debris and the projectile were safely contained during the experiment. The box was fitted with two 3.175 mm thick clear polycarbonate panels, allowing to safely place the ultra high-speed camera outside of the catcher box while still being able to record the impact event.

A sample holder consisting of two 10 mm tall blocks that ran along the impact direction was used. The blocks are spaced such that the sample can lightly be held in place in between them, such that it was not clamped. This allowed the sample to displace along the impact direction while avoiding any undesired stresses along the edge of the specimen and also preventing it from tilting out-of-plane.

From Fig. 1, it can be seen that strain gages were bonded to the samples. The strain gage has two purposes. First, the strain gage allows for the monitoring of the imparted loading onto the samples, measuring the imparted stress wave from impact for each experiment, thus ensuring repeatability between consecutive experiments. Second, the strain gage is used to trigger the ultra high-speed camera. This is possible since a noticeable voltage change is produced as the compressive wave passes through the strain gage, which is

used as a trigger signal, allowing for the precise triggering of the camera.

For an isotropic material, a crack loaded under mode-II conditions will not remain in pure mode-II conditions and would grow under mixed mode conditions [7]. However, in this case, the material is anisotropic, and the notch and all the fibers are oriented along the same direction. The fiber/matrix interface acts as a weak plane that allows for the crack to remain under mode-II conditions upon propagation [4, 19].

Imaging Techniques

The ultra high-speed camera used in this study is a Shimadzu HPV-X2. This camera has a resolution of 400 pixels \times 250 pixels, and is able to record 128 frames at up to 5,000,000 frames per second (fps) at full resolution. For this experiment frame rates of 1,000,000 fps and 1,500,000 fps were used at full resolution. The number of frames recorded by this type of camera is fixed, meaning that at 1,000,000 fps the recording window is 128 μ s, hence the need to use a very precise triggering mechanism (here the strain gage bonded to the sample).

The camera was carefully aligned to be orthogonal to the sample to properly capture the in-plane behavior of the sample when using 2-D digital image correlation as the sample fractures, see Fig. 2. The area of interest was lit with two high-intensity LEDs as shown in Fig. 2 to achieve the adequate exposure necessary in the high frame rate regime used.

DIC is used in conjunction with the ultra high-speed camera to obtain full-field vertical and horizontal displacement fields of the fracture samples during the entirety of

the fracture event. The samples were prepared for DIC by applying a coat of white paint and hand-speckling them with black dots as shown in Fig. 3. Hand-speckling was chosen over spray painting due to spray painting having a risk of generating uneven patterns and too small speckles given the camera resolution at hand.

The recorded area has a size of 88 mm \times 55 mm, see Fig. 1, with an average pixel size of 0.22 mm/px. VIC-2D was used to perform the DIC correlation, and the parameters used for the correlation are shown in Table 2. Fig. 3 shows three columns displaying the images recorded from the ultra high-speed camera, and the horizontal and shear strain fields generated by the DIC algorithm for four different time instants (8 μ s, 18 μ s, 28 μ s and 43 μ s) with time $t = 0 \mu$ s corresponding to the time of impact.

It should be noted that although strain fields were also obtained from DIC they were not used to obtain the stress intensity factors due to strains having a high inherent error. The reason being the main output from any DIC engine are displacements, the strains are calculated by using the output displacements, adding an extra step, furthermore the amount of displacement points used to calculate a single strain point could also smooth out features or add noise to the results. All strain results values shown in this study were obtained using a virtual strain gage of 6 mm. Meaning that even though DIC will give a strain value at every pixel, that data point corresponds to a 6 mm \times 6 mm area.

Stress Intensity Factors

It has been well established that the displacements around a crack-tip for an anisotropic material can be related to the stress intensity factors at the crack-tip [22]. These relationships are shown in Eqs. (1) and (2),

$$u = K_I \sqrt{\frac{2r}{\pi}} \operatorname{Re} \left[\frac{1}{\mu_2 - \mu_1} (p_1 \mu_2 z_1 - p_2 \mu_1 z_2) \right] + K_{II} \sqrt{\frac{2r}{\pi}} \operatorname{Re} \left[\frac{1}{\mu_2 - \mu_1} (p_1 z_1 - p_2 z_2) \right] + T_x - Rr \sin \theta, \quad (1)$$

$$v = K_I \sqrt{\frac{2r}{\pi}} \operatorname{Re} \left[\frac{1}{\mu_2 - \mu_1} (q_1 \mu_2 z_1 - q_2 \mu_1 z_2) \right] + K_{II} \sqrt{\frac{2r}{\pi}} \operatorname{Re} \left[\frac{1}{\mu_2 - \mu_1} (q_1 z_1 - q_2 z_2) \right] + T_y + Rr \cos \theta, \quad (2)$$

where,

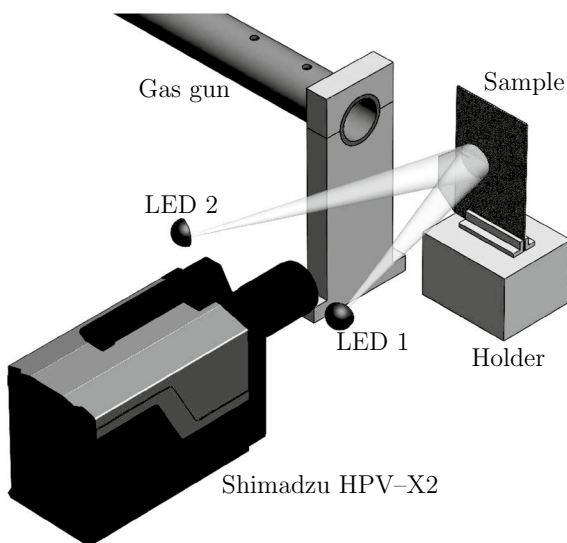


Fig. 2 Digital image correlation experimental setup. Not shown: catcher box

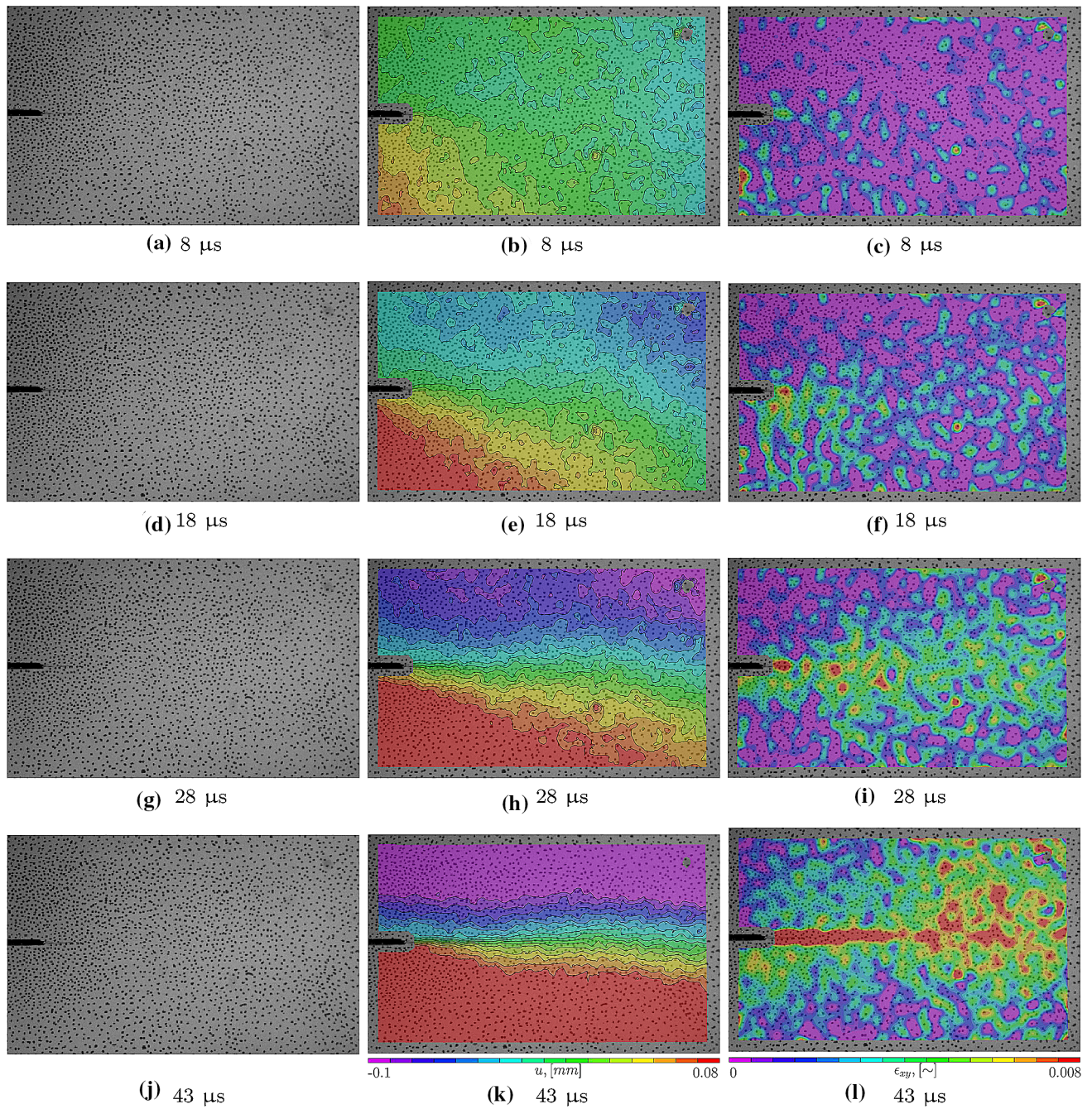


Fig. 3 Left column: footage obtained from the ultra high-speed camera. Middle column: horizontal displacement fields obtained from DIC. Right column: shear strain fields obtained from DIC. Here, $t = 0 \mu s$ corresponds to the impact instant. The crack starts to grow at $t = 28 \mu s$ in the pictured experiment

Table 2 DIC parameters

Camera model	Shimadzu HPV-X2
Sensor array size	400 px × 250 px
Scale factor	0.22 mm/px
Program	Vic-2D 6
Subset size	15 px
Step size	1 px
Criterion	Zero-mean normalized sum of square difference (ZNSSD)
Interpolation	Optimized 8-tap
Strain filter	15
Virtual strain gage	6 mm

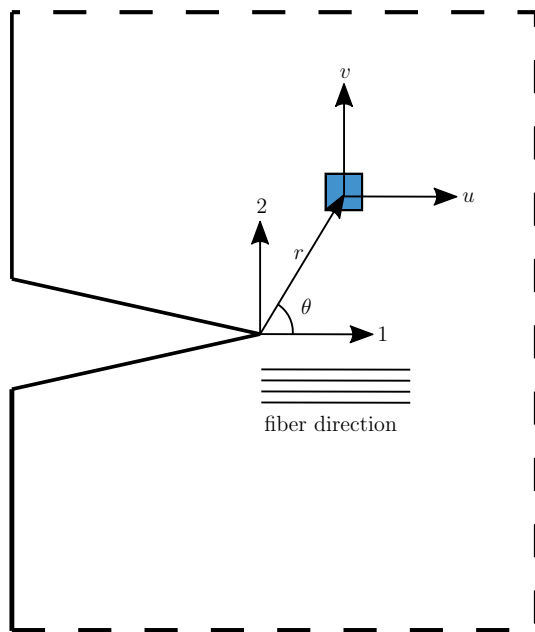


Fig. 4 Crack-tip coordinate system

$$p_j = \mu_j^2 S_{11} + S_{12} - \mu_j S_{16},$$

$$q_j = \mu_j S_{12} + \frac{S_{22}}{\mu_j} - S_{26},$$

$$z_j = \sqrt{\cos \theta + \mu_j \sin \theta},$$

and $\mu_j (j = 1, 2)$ are the two roots of:

$$S_{11}\mu^4 - 2S_{16}\mu^3 + (2S_{12} + S_{66})\mu^2 - 2S_{26}\mu + S_{22} = 0.$$

Here, u and v are the horizontal and vertical displacements, respectively, S_{ij} is the in-plane compliance matrix of the material, K_I and K_{II} are the mode-I and mode-II stress

intensity factors, r and θ are the polar coordinates from the crack-tip, and T_x , T_y and R are added terms to account for rigid body translation and rotation of the sample.

These equations can be applied to every frame of footage obtained in the experiment. Displacements, u and v , are obtained for every pixel location from DIC. The compliance matrix S_{ij} was obtained by characterizing the material, with the 1-direction being the fiber direction. Fig. 4 shows the polar coordinates used to define the location of each pixel, meaning that every pixel will be associated with displacement information as well as polar coordinate values. Therefore, for every frame there will be an over-determined system of equations with as many equations as twice the amount of pixels selected where the only unknowns are K_I , K_{II} , T_x , T_y , and R . This system of equations can then be solved by performing a least-squares regression [9, 24].

It has been shown by Kirugulige and Tippur [9] and Yoneyama et al. [24] that by transforming Eqs. (1) and (2) from cartesian displacements into polar displacements the accuracy of the results obtained from a least-squares analysis can be improved. Hence the following transformation is applied,

$$\begin{Bmatrix} u_r \\ u_\theta \end{Bmatrix} = \begin{bmatrix} \cos \theta & \sin \theta \\ -\sin \theta & \cos \theta \end{bmatrix} \begin{Bmatrix} u \\ v \end{Bmatrix}$$

and thus, Eq. (3) is obtained,

$$u_r = [f(r, \theta) \cos \theta + h(r, \theta) \sin \theta] K_I + [g(r, \theta) \cos \theta + l(r, \theta) \sin \theta] K_{II} + T_x \cos \theta + T_y \sin \theta. \tag{3}$$

Here, the functions f , g , h , and l are condensed forms of the terms found in Eqs. (1) and (2). Equation. (3) shows the radial displacement as a function of K_I , K_{II} , T_x , and T_y , and the resulting system has as many equations as pixels selected. It must be noted that an equation using the tangential displacement, u_θ , can be obtained as well, however it has been proven by Kirugulige and Tippur [9] that radial displacements produce more accurate results.

Crack-Tip Location

It is apparent from Eqs. (1), (2) or (3) that having the crack-tip location is critical for the proper calculation of the stress intensity factor. In this case the original location of the crack was known beforehand. However, the task of accurately determining the instant at which the crack starts to grow is not as straightforward as it perhaps may seem.

Due to the Shimadzu HPV-X2 camera’s limited resolution (400 px × 250 px), the apparent crack-tip location is not necessarily the actual crack-tip location. This discrepancy

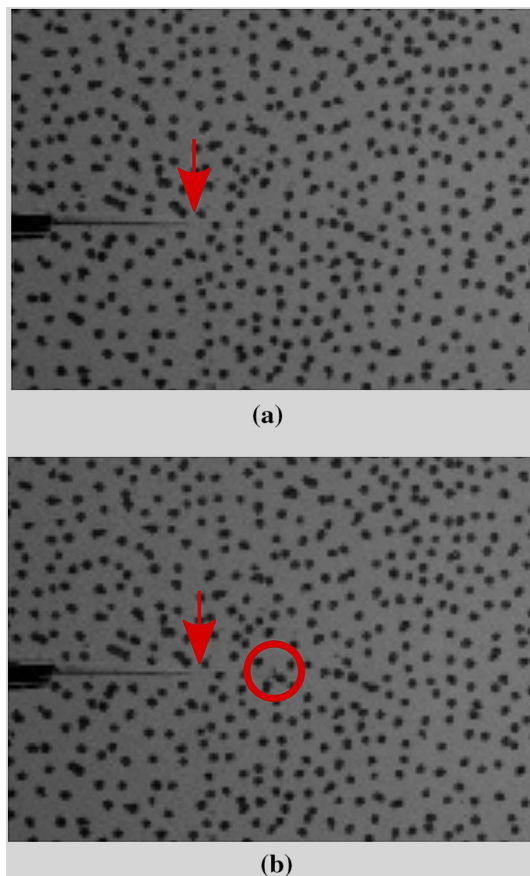


Fig. 5 a Apparent crack-tip location. b Apparent crack tip location versus possible crack-tip location

can be observed in Fig. 5, where Fig. 5a shows the unloaded sample and the crack tip location is highlighted by an arrow. Figure 5b shows a frame taken during the fracture event and it can be seen that the crack tip seems to not have moved. However, fiber breakage, highlighted in the circle, indicates that the crack has already started growing.

Since in the case studied here, mode-II fracture, the crack will grow under shear, there will not be significant crack opening, making it cumbersome to visually identify the location of the crack once it starts to grow. However, there will be significant sliding motion, in particular above and below the crack. As such, the horizontal displacement directly below the crack tip (loaded half) was evaluated as well as the shear strain directly in front of the crack. In addition the average displacement of the impacted half was also extracted from DIC, all these quantities are shown in Fig. 6.

It was observed that the horizontal displacement below the crack-tip showed different behaviors before and after the crack initiation. In Fig. 7 the horizontal displacement directly below the crack tip was plotted with respect to time for a dry sample. Results show that the displacement increases steadily, as expected, and at a given time, the displacement plateaus and then starts increasing again at a faster rate due to the bottom half of the sample sliding. Additionally, visual evidence of crack growth was observed and has been highlighted in red during the plateau region and after. This type of behavior was observed for all samples.

Next, the shear strains directly in front of the crack tip where obtained and plotted with respect to the overall horizontal displacement of the impacted half of the

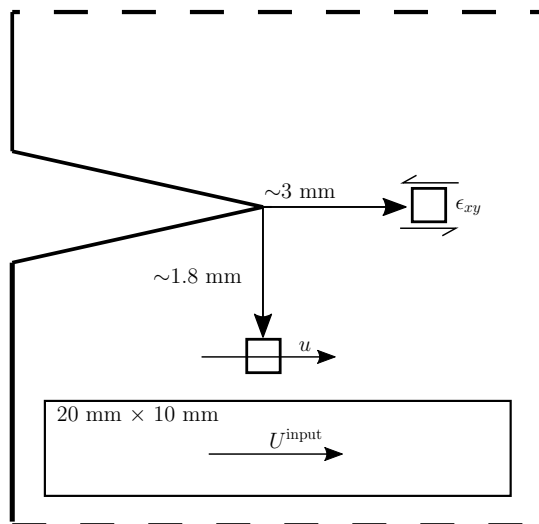


Fig. 6 Extracted variables from DIC: ϵ_{xy} is the shear strain at point 3 mm ahead of the crack-tip; u is the horizontal displacement at a point 1.8 mm below the crack-tip; and U^{input} is the horizontal input displacement due to impact over an area of 20 mm \times 10 mm below the crack tip. All displacement had their rigid body motion removed by DIC. Not to scale

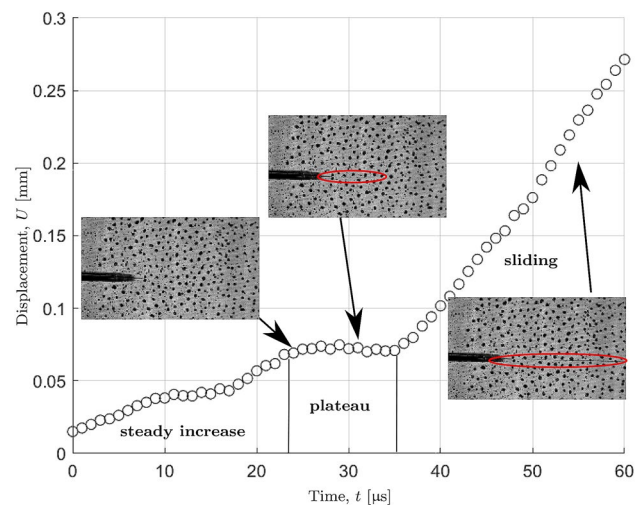


Fig. 7 Displacement directly below the crack tip versus time for a dry sample. Shown are three different behaviors that were related to crack growth. Circled in red is visual evidence of crack growth

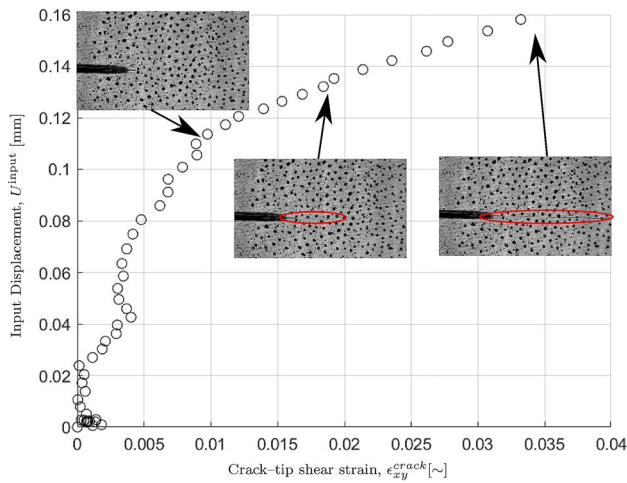


Fig. 8 Shear strain in front of crack tip versus input displacement from impact. Circled in red is visual evidence of crack growth

sample. The behavior of this plot was similar to that of a stress-strain curve, with an initial linear-like behavior following a plastic-like behavior as shown in Fig. 8. In this case the input displacement would be directly correlated to the load being imparted into the sample, or the stress being experienced by the sample. The shear strain extracted was obtained 3 mm in front of the crack-tip (half a virtual strain gage). While the input displacement was obtained

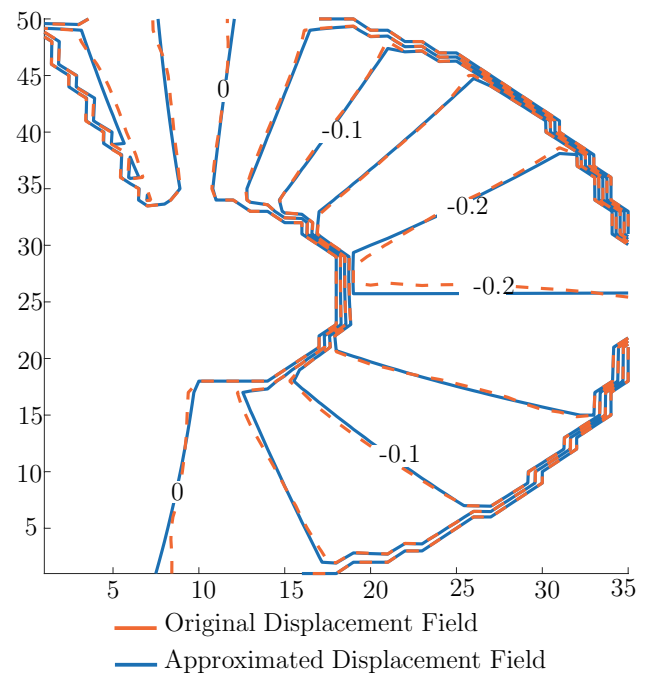


Fig. 9 DIC (in dashed orange) and approximated (in blue) radial displacement fields. Axes are in pixels, contours are in mm (Color figure online)

by averaging the horizontal displacement points below the notch over an area of 20 mm × 10 mm.

Table 3 Average critical mode-II stress intensity factors for all types of samples at different angular sweeps

θ Sweep range	Dry	Soaked	Naturally aged
$\pm 135^\circ$	$33.6 \pm 4.4 \text{ MPa}\sqrt{\text{m}}$	$26.4 \pm 3.1 \text{ MPa}\sqrt{\text{m}}$	$24.6 \pm 1.0 \text{ MPa}\sqrt{\text{m}}$
$\pm 124^\circ$	$35.1 \pm 3.2 \text{ MPa}\sqrt{\text{m}}$	$26.5 \pm 3.3 \text{ MPa}\sqrt{\text{m}}$	$24.9 \pm 0.9 \text{ MPa}\sqrt{\text{m}}$
$\pm 113^\circ$	$35.8 \pm 2.6 \text{ MPa}\sqrt{\text{m}}$	$26.4 \pm 3.5 \text{ MPa}\sqrt{\text{m}}$	$24.9 \pm 0.9 \text{ MPa}\sqrt{\text{m}}$
$\pm 101^\circ$	$36.2 \pm 2.6 \text{ MPa}\sqrt{\text{m}}$	$26.0 \pm 3.7 \text{ MPa}\sqrt{\text{m}}$	$24.4 \pm 1.5 \text{ MPa}\sqrt{\text{m}}$
$\pm 90^\circ$	$36.6 \pm 3.3 \text{ MPa}\sqrt{\text{m}}$	$25.3 \pm 3.7 \text{ MPa}\sqrt{\text{m}}$	$23.7 \pm 2.3 \text{ MPa}\sqrt{\text{m}}$

The values shown here were calculated using a radial sweep of $0.85 \leq r/t \leq 2.5$

Table 4 Average critical mode-II stress intensity factors for all types of samples at different r_{max}/t -values

Maximum r/t	Dry	Soaked	Naturally aged
3.0	$37.1 \pm 2.8 \text{ MPa}\sqrt{\text{m}}$	$27.2 \pm 4.5 \text{ MPa}\sqrt{\text{m}}$	$25.5 \pm 0.4 \text{ MPa}\sqrt{\text{m}}$
2.5	$35.8 \pm 2.6 \text{ MPa}\sqrt{\text{m}}$	$26.4 \pm 3.5 \text{ MPa}\sqrt{\text{m}}$	$24.9 \pm 0.9 \text{ MPa}\sqrt{\text{m}}$
2.0	$34.3 \pm 3.6 \text{ MPa}\sqrt{\text{m}}$	$25.2 \pm 2.8 \text{ MPa}\sqrt{\text{m}}$	$24.1 \pm 2.2 \text{ MPa}\sqrt{\text{m}}$
1.5	$33.2 \pm 7.2 \text{ MPa}\sqrt{\text{m}}$	$23.4 \pm 6.0 \text{ MPa}\sqrt{\text{m}}$	$23.3 \pm 3.2 \text{ MPa}\sqrt{\text{m}}$

All values with an angular sweep of $-113^\circ \leq \theta \leq 113^\circ$

Fig. 10 Stress intensity factor histories for different experiments up until the moment of fracture. Impact occurs at $t = 0$. The different experiments are highlighted by different symbols

Results

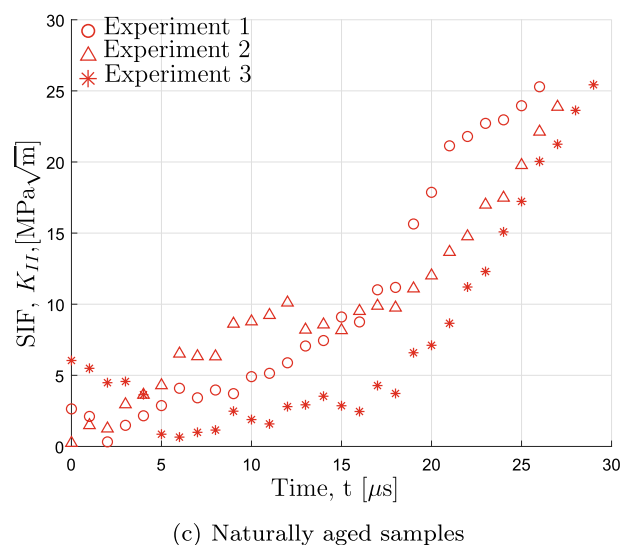
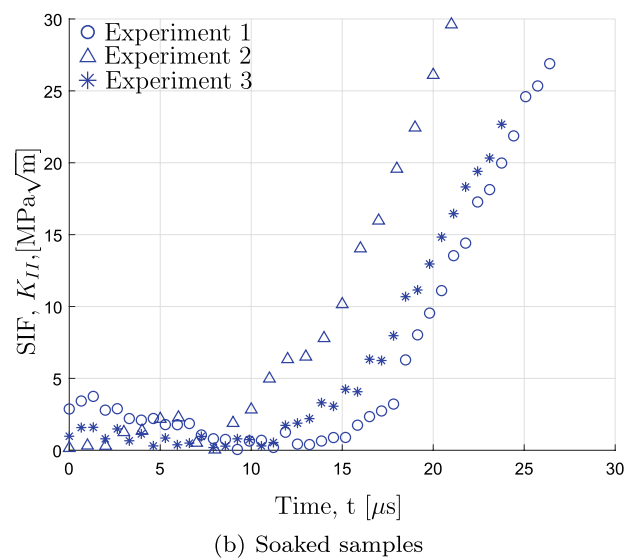
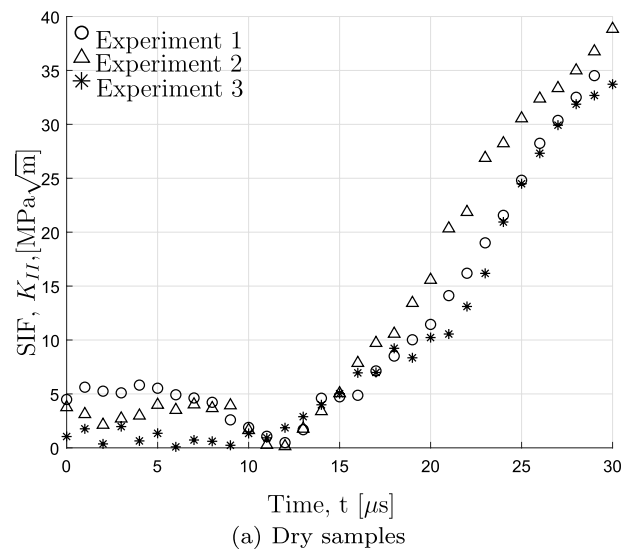
When obtaining the stress intensity factor through the methods described earlier it must be noted that the neighborhood of pixels used in the least-squares regression must be picked carefully, as Eq. (3) does not account for boundary effects and assumes an idealized crack with zero thickness. As demonstrated by Shannahan [20] the neighborhood of points selected can have a significant effect on the values for stress intensity factor obtained. This is because the least-squares regression is performing an approximation based on the given data points. Therefore, the SIF was obtained for different ranges of radius, r , and angle, θ . A minimum normalized radial value of $0.85 < r/t$ was used, where r is the radius and t the laminate thickness. The minimum radial value was chosen such that any point picked would be at least half a subset away from the crack tip. No points within a half a subset radius were picked, since DIC would treat this region as a continuous surface, rather than a discontinuous one, and this translates in the displacements not being properly calculated. Additionally, it has been widely reported that values too close to the crack-tip should not be used because they will be affected by plastic and 3-D effects [11, 20].

Radial sweeps between $0.85 \leq r/t \leq r_{max}/t$ were performed and studied, where r_{max}/t ranged between 1.5 and 3.0. Additionally, angular sweeps between $-90^\circ < \theta < 90^\circ$ and $-135^\circ < \theta < 135^\circ$ were performed. The average critical mode-II stress intensity factors obtained in all these cases are summarized in Tables 3 and 4.

The critical stress intensity factor values changed depending on what neighborhood sweep was selected. No literature was found with expected values for dynamic mode-II critical stress intensity factors for carbon fiber/epoxy laminates. As such, it was observed if the different critical SIF values converged towards a set value. Maximum r/t values of 3.0, 2.5 and 2.0 giving acceptable results. However radial sweeps between $0.85 \leq r/t \leq 1.5$, gave a variation in ranges of SIF that seemed non-physical and therefore were discarded.

Remaining results show consistency in that the critical SIF for the dry samples is always higher than the SIF for the conditioned samples, and that the critical SIF for the dry samples is about 30% higher than that of the conditioned samples. Even though the soaked samples have slightly higher values than the naturally aged samples, the difference is not significant given the spread of the results.

To corroborate that the least-squares regression was properly executed, care was taken ensure that the values of K_I , K_{II} , T_x and T_y obtained from the regression would return the same displacement fields as those obtained from DIC when



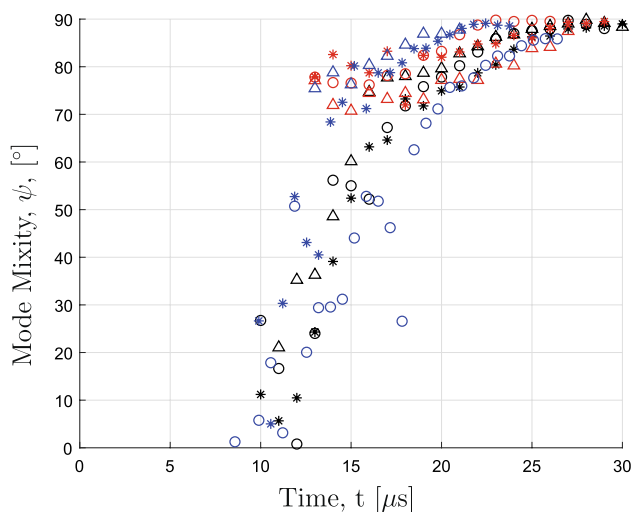


Fig. 11 Mode mixity for all experiments. Dry samples highlighted in black, soaked samples in blue and naturally aged samples in red. Different experiments highlighted by different symbols. Impact occurs at $t = 0$ and crack growth initiation at $t \approx 30 \mu\text{s}$ (Color figure online)

plugged back into Eq. (3). Figure 9 shows the displacement fields obtained from DIC (in orange), and from the least-squares regression (in blue) of a sample at the instant right before crack growth occurs. The process employed reproduced the displacement fields inputted, with a negligible error.

The stress intensity factor histories until crack growth initiation were extracted for all samples. Figure 10 shows the SIF histories using a neighborhood of $0.85 < r/t < 2.5$ and $-113^\circ \leq \theta \leq 113^\circ$. As expected, the samples show a steady increase in SIF until the moment of crack initiation. No significant features are observed before or after the crack starts to grow. Hence, it was necessary to find a reliable method of determining the moment of crack growth initiation without relying on visual cues. Fig. 10a–c shows that it took 25–30 μs for the cracks to start growing, which is in agreement with the observations made by Coker and Rosakis when performing similar experiments on carbon fiber/epoxy samples [4]. Furthermore, the stress wave released upon impact does not travel uniformly through the sample and it takes approximately 10 μs for the crack to be properly asymmetrically loaded.

In Fig. 11 the mode mixity, ψ , was plotted for every sample, to corroborate that the experimental mode-II loading conditions were indeed achieved. As a reference $\psi = \tan^{-1}(K_{II}/K_I)$, and from this equation it is clear that the higher the value of ψ , the closer the experiment is to pure mode-II loading, and similarly, the closer it gets to pure mode-I loading the closer ψ gets to zero. As shown in Fig. 11, ψ increases towards 90° and at the moment of crack growth initiation $\psi \approx 90^\circ$ for all experiments, confirming

that the experimental setup used provides a predominantly mode-II loading of the crack.

As previously mentioned in the “Crack-Tip Location” section the horizontal displacement directly below the crack-tip (see Fig. 6) was extracted for each sample and plotted with respect to time. The displacements extracted had their rigid body motion removed by DIC, so that only the displacement induced from the impact would be observed. These extractions are plotted in Fig. 12, for all experiments. The moment of crack growth initiation is indicated by a green dot. All the samples exhibit similar behaviors and similar fracture instants.

Next, the shear strain was plotted against the input displacement curves for all experiments, see Fig. 13. Two things must be remembered. First, after crack initiation the shear values should not be taken as physical values, since they are being calculated assuming a continuous medium, however the crack has already started growing, introducing a discontinuity. Second, these values are more prone of including error due to hardware limitations, such as inherent camera noise and limited spatial resolution of the camera. Therefore, these plots should be analyzed qualitatively rather than quantitatively.

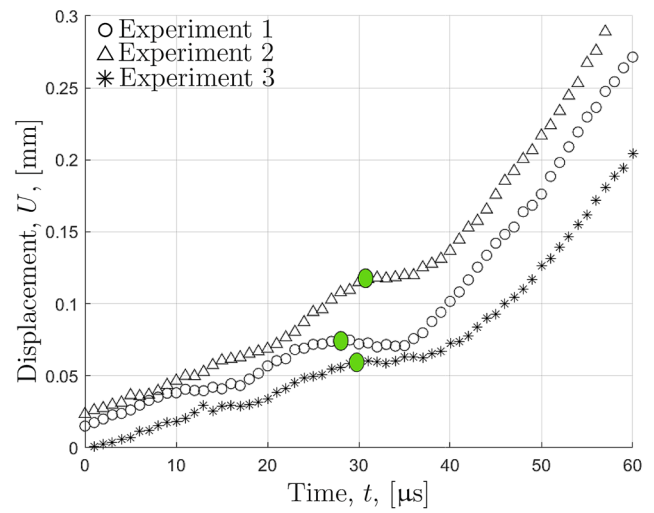
It was observed that for all samples the moment of crack initiation corresponds to the moment of change in behavior for both displacement and shear curves, as shown in the plots in Figs. 12 and 13. This can be explained due to the fact that once the crack starts to grow, the behavior in the vicinity of the crack-tip will change. For example, once the crack starts to grow there will be a high amount of sliding motion due to the presence of the crack. In turn, the DIC engine will treat this as a region with high levels of shear, leading to the high strain levels observed.

Conclusions

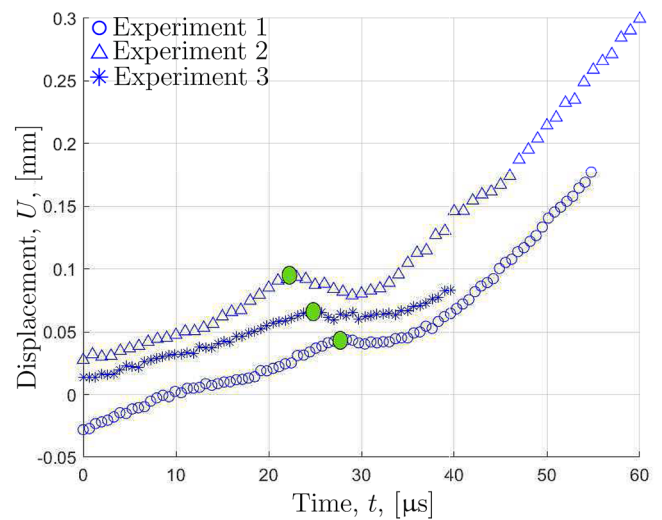
This study showed how moisture intake can have a detrimental effect on the mode-II critical stress intensity factor of carbon fiber/epoxy specimens. It was observed that after the matrix dominated material properties of the specimens prepared degraded due to moisture absorption, as expected, the dynamic mode-II stress intensity factors also presented degradation.

The experimental setup used successfully obtained predominant mode-II conditions, with little to non mode-I loading present at the crack-tip. Results showed that dry carbon fiber epoxy specimens had a consistently higher mode-II critical stress intensity factor than the aged samples, almost 30% higher. This behavior was as expected and follows previous findings on water absorption leading to a decrease in performance of fiber reinforced polymers, in this case fracture toughness. Since in this case the failure mechanism

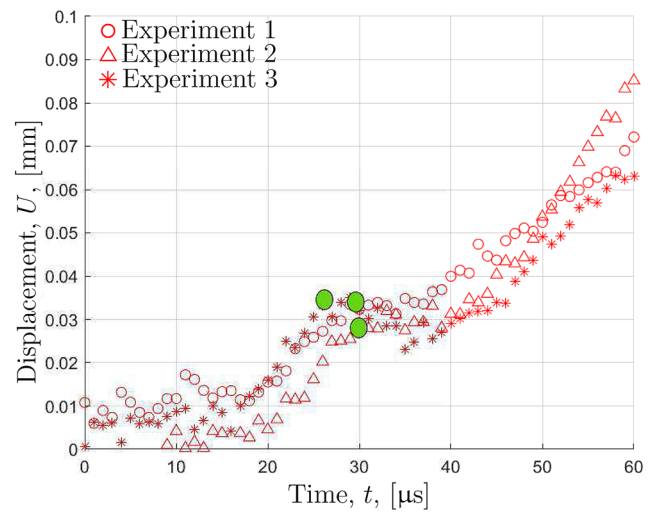
Fig. 12 Horizontal displacement directly below of the crack-tip history. Different experiments are shown with different markers. Crack growth initiation is indicated by green circle (Color figure online)



(a) Dry samples

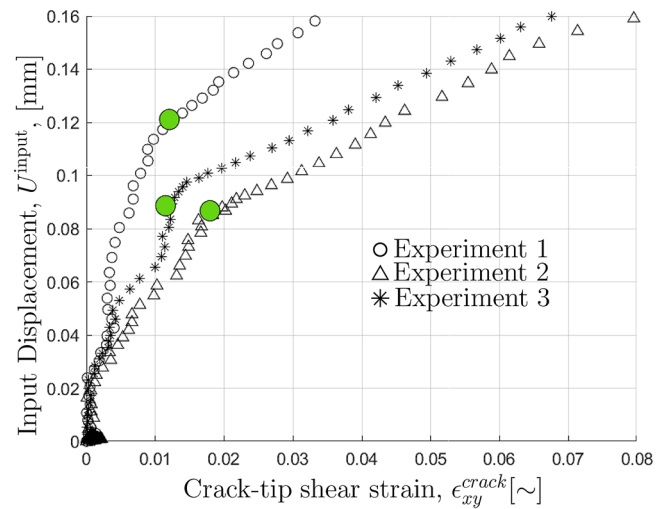


(b) Soaked samples

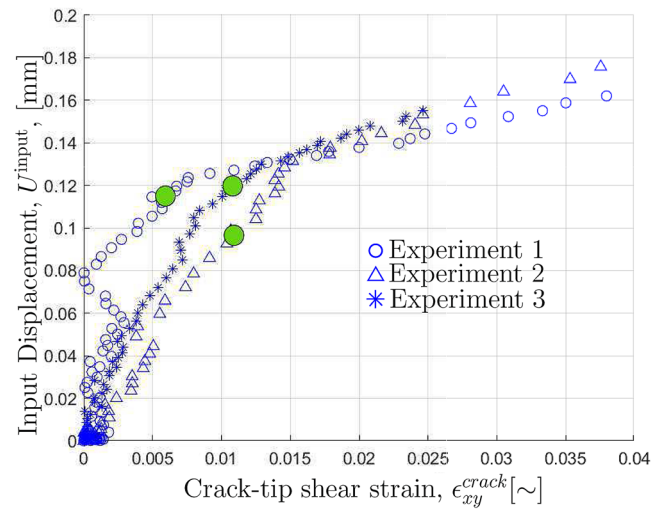


(c) Naturally aged Samples

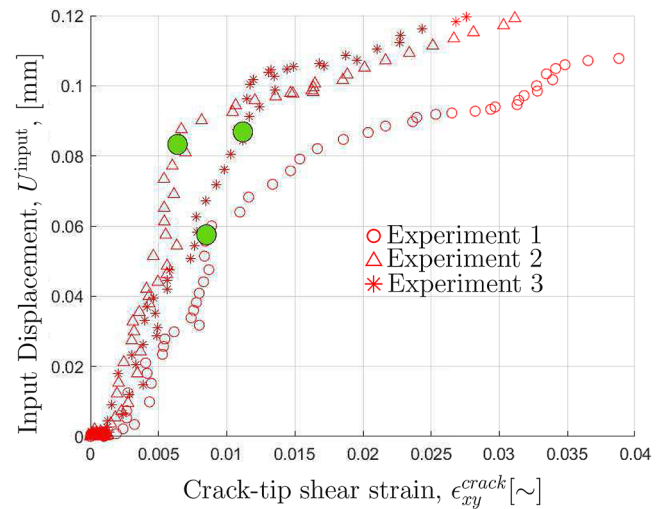
Fig. 13 Shear strain in front of the crack tip vs. input displacement generated from impact. Different experiments are shown with different markers. Crack growth initiation is indicated by green circle. For all experiments the behavior of the plot changes after fracture occurs (Color figure online)



(a) Dry samples



(b) Soaked samples



(c) Naturally aged samples

is shear along the fiber/matrix interface, it can be concluded that the effect moisture has on the matrix of the composite led to this degradation, and this is further reinforced by the in-plane shear modulus of the composite also experiencing a degradation of a similar magnitude.

Additionally, no apparent difference between hygrothermally aged samples and naturally aged samples was found. Showing the time of submersion and temperatures up to 65 °C did not have a considerable impact on the mode-II fracture toughness of T-700 carbon fiber/epoxy laminates.

It was also observed that for all samples there were noticeable changes in behavior near the crack-tip that were used to identify the time instant of crack growth initiation. In particular the displacement directly below the crack-tip signaled the onset of crack growth and the moment at which the bottom half started to slide, and the shear strain right in front of the crack-tip showed different behaviors before and after crack growth initiation. Finally, it was also observed that all samples, regardless of conditioning, fractured 30 μs after impact.

Acknowledgements The authors would like to thank the Office of Naval Research through Grant Number N00014-16-1-3215. Special thanks to the program manager Dr. Y.D.S. Rajapakse. We would also like to thank Professor H. Kim from UC San Diego and the students in his group for their invaluable help. We also want to thank Kaneka Composites for donating the epoxy used in making the carbon fiber specimens.

Funding This study was funded by Office of Naval Research through Grant Number N00014-16-1-3215.

Compliance with Ethical Standards

Conflict of interest The authors declare that they have no conflict of interest.

References

- Arora H, Hooper P, Dear J (2011) Dynamic response of full-scale sandwich composite structures subject to air-blast loading. *Composites A* 42(11):1651–1662
- Arora H, Rolfé E, Kelly M, Dear JP (2017) Full-scale air and underwater-blast loading of composite sandwich panels. *Explosion blast response of composites*, chap 7. Woodhead Publishing, Cambridge, pp 161–199
- Broughton WR, Maxwell AS (2007) Measurement good practice guide No. 103: accelerated environmental ageing of polymeric materials. Tech. rep., National Physical Laboratory
- Coker D, Rosakis AJ (2001) Experimental observations of intersonic crack growth in asymmetrically loaded unidirectional composite plates. *Philos Mag A* 81(3):571–595
- Fitriah SN, Abdul Majid MS, Ridzuan MJ, Daud R, Gibson AG, Assaleh TA (2017) Influence of hydrothermal ageing on the compressive behaviour of glass fibre/epoxy composite pipes. *Compos Struct* 159:350–360
- Guerhazi N, Ben Tarjem A, Ksouri I, Ayedi HF (2016) On the durability of FRP composites for aircraft structures in hygrothermal conditioning. *Composites B* 85:294–304
- Kalthoff JF (2000) Modes of dynamic shear failure in solids. *Int J Fract* 101(1):1–31. <https://doi.org/10.1023/A:1007647800529>
- Kelly M, Arora H, Worley A, Kaye M, Linz PD, Hooper PA, Dear JP (2016) Sandwich panel cores for blast applications: materials and graded density. *Exp Mech* 56(4):523–544
- Kirugulige MS, Tippur HV (2009) Measurement of fracture parameters for a mixed-mode crack driven by stress waves using image correlation technique and high-speed digital photography. *Strain* 45(2):108–122
- Koohbor B, Mallon S, Kidane A, Sutton MA (2014) A DIC-based study of in-plane mechanical response and fracture of orthotropic carbon fiber reinforced composite. *Composites B* 66:388–399
- Lee D, Tippur H, Kirugulige M, Bogert P (2009) Experimental study of dynamic crack growth in unidirectional graphite/epoxy composites using digital image correlation method and high-speed photography. *J Compos Mater* 43(19):2081–2108
- Lee D, Tippur H, Bogert P (2010) Quasi-static and dynamic fracture of graphite/epoxy composites: an optical study of loading-rate effects. *Composites B* 41(6):462–474
- Lindblom F (2003) Use of composites in the Bisby class stealth corvette. In: *ACMC/SAMPE conference on marine composites*, pp 11–12. Plymouth
- Mallon S, Koohbor B, Kidane A, Sutton MA (2015) Fracture behavior of prestressed composites subjected to shock loading: a dic-based study. *Exp Mech* 55(1):211–225
- Matos H, Javier C, LeBlanc J, Shukla A (2018) Underwater near-field blast performance of hydrothermally degraded carbon-epoxy composite structures. *Multiscale Multidiscip Model Exp Des* 1(1):33–47
- Mouritz A (2001) Ballistic impact and explosive blast resistance of stitched composites. *Composites B* 32(5):431–439
- Mouritz A, Gellert E, Burchill P, Challis K (2001) Review of advanced composite structures for naval ships and submarines. *Compos Struct* 53(1):21–42
- Rolfé E, Quinn R, Sancho A, Kaboglu C, Johnson A, Liu H, Hooper PA, Dear JP, Arora H (2018) Blast resilience of composite sandwich panels with hybrid glass-fibre and carbon-fibre skins. *Multiscale Multidiscip Model Exp Des* 1(3):197–210
- Rosakis AJ (1999) Cracks faster than the shear wave speed. *Science* 284(5418):1337–1340
- Shannahan LS (2017) A hybrid experimental-computational approach for the analysis of dynamic fracture. Ph.D. thesis, Drexel University
- Shillings C, Javier C, LeBlanc J, Tilton C, Corvese L, Shukla A (2017) Experimental and computational investigation of the blast response of Carbon-Epoxy weathered composite materials. *Composites B* 129:107–116
- Sih GC, Paris PC, Irwin GR (1965) On cracks in rectilinearly anisotropic bodies. *Int J Fract Mech* 1(3):189–203
- Tekalur SA, Shukla A, Shivakumar K (2008) Blast resistance of polyurea based layered composite materials. *Compos Struct* 84(3):271–281
- Yoneyama S, Morimoto Y, Takashi M (2006) Automatic evaluation of mixed-mode stress intensity factors utilizing digital image correlation. *Strain* 42(1):21–29

Publisher's Note Springer Nature remains neutral with regard to jurisdictional claims in published maps and institutional affiliations.